Monthly Notices
of the
ROYAL ASTRONOMICAL SOCIETY

MNRAS **464**, 3636–3656 (2017) doi:10.1093/mnras/stw2531
Advance Access publication 2016 October 4

The *Hubble Space Telescope* UV Legacy Survey of Galactic globular clusters – IX. The Atlas of multiple stellar populations

A. P. Milone,[1⋆] G. Piotto,[2,3] A. Renzini,[3] A. F. Marino,[1] L. R. Bedin,[3] E. Vesperini,[4] F. D'Antona,[5] D. Nardiello,[2] J. Anderson,[6] I. R. King,[7] D. Yong,[1] A. Bellini,[6] A. Aparicio,[8,9] B. Barbuy,[10] T. M. Brown,[6] S. Cassisi,[11] S. Ortolani,[2] M. Salaris,[12] A. Sarajedini[13] and R. P. van der Marel[6]

[1]*Research School of Astronomy and Astrophysics, Australian National University, Mt Stromlo Observatory, via Cotter Rd, Weston, ACT 2611, Australia*
[2]*Dipartimento di Fisica e Astronomia 'Galileo Galilei', Univ. di Padova, Vicolo dell'Osservatorio 3, Padova I-35122, Italy*
[3]*Istituto Nazionale di Astrofisica – Osservatorio Astronomico di Padova, Vicolo dell'Osservatorio 5, Padova I-35122, Italy*
[4]*Department of Astronomy, Indiana University, Bloomington, IN 47405, USA*
[5]*Istituto Nazionale di Astrofisica – Osservatorio Astronomico di Roma, Via Frascati 33, I-00040 Monteporzio Catone, Roma, Italy*
[6]*Space Telescope Science Institute, 3800 San Martin Drive, Baltimore, MD 21218, USA*
[7]*Department of Astronomy, University of Washington, Box 351580, Seattle, WA 98195-1580, USA*
[8]*Instituto de Astrofisica de Canarias, E-38200 La Laguna, Tenerife, Canary Islands, Spain*
[9]*Department of Astrophysics, University of La Laguna, E-38200 La Laguna, Tenerife, Canary Islands, Spain*
[10]*IAG, Universidade de Sao Paulo, Rua de Matao 1226, Ciudade Universitaria, Sao Paulo 05508-900, Brazil*
[11]*Istituto Nazionale di Astrofisica – Osservatorio Astronomico di Teramo, Via Mentore Maggini s.n.c., I-64100 Teramo, Italy*
[12]*Astrophysics Research Institute, Liverpool John Moores University, Liverpool Science Park, IC2 Building, 146 Brownlow Hill, Liverpool L3 5RF, UK*
[13]*Department of Astronomy, University of Florida, 211 Bryant Space Science Center, Gainesville, FL 32611, USA*

Accepted 2016 October 3. Received 2016 September 29; in original form 2016 July 22; Editorial Decision 2016 September 29

ABSTRACT

We use high-precision photometry of red-giant-branch (RGB) stars in 57 Galactic globular clusters (GCs), mostly from the '*Hubble Space Telescope* (*HST*) UV Legacy Survey of Galactic GCs', to identify and characterize their multiple stellar populations. For each cluster the pseudo-two-colour diagram (or 'chromosome map') is presented, built with a suitable combination of stellar magnitudes in the *F*275*W*, *F*336*W*, *F*438*W*, and *F*814*W* filters that maximizes the separation between multiple populations. In the chromosome map of most GCs (type-I clusters), stars separate in two distinct groups that we identify with the first (1G) and the second generation (2G). This identification is further supported by noticing that 1G stars have primordial (oxygen-rich, sodium-poor) chemical composition, whereas 2G stars are enhanced in sodium and depleted in oxygen. This 1G–2G separation is not possible for a few GCs where the two sequences have apparently merged into an extended, continuous sequence. In some GCs (type-II clusters) the 1G and/or the 2G sequences appear to be split, hence displaying more complex chromosome maps. These clusters exhibit multiple subgiant branches (SGBs) also in purely optical colour–magnitude diagrams, with the fainter SGB joining into a red RGB which is populated by stars with enhanced heavy-element abundance. We measure the RGB width by using appropriate colours and pseudo-colours. When the metallicity dependence is removed, the RGB width correlates with the cluster mass. The fraction of 1G stars ranges from ∼8 per cent to ∼67 per cent and anticorrelates with the cluster mass, indicating that incidence and complexity of the multiple population phenomenon both increase with cluster mass.

Key words: techniques: photometric – stars: abundance – stars: Population II – globular clusters: general.

⋆ E-mail: antonino.milone@anu.edu.au

1 INTRODUCTION

The formation of globular clusters (GCs) and the origin of their ubiquitous multiple stellar populations remain a major astrophysical challenge. In this series of papers, we build on the *Hubble Space Telescope* (*HST*) UV Legacy Survey of Galactic GCs (Piotto et al. 2015, hereafter Paper I of this series) to fully document the complexity of the multiple populations. This phenomenon is most effectively characterized when combining ultraviolet and optical *HST* photometry, as documented by pilot studies by our group (e.g. Milone et al. 2012b, 2013; Piotto et al. 2013). These studies have demonstrated that appropriate combinations of ultraviolet and optical filters, to construct e.g. $m_{F275W} - m_{F336W}$ versus $m_{F336W} - m_{F438W}$ two-colour diagrams or the m_{F814W} plot versus the pseudo-colour $C_{F275W,\,F336W,\,F438W} = (m_{F275W} - m_{F336W}) - (m_{F336W} - m_{F438W})$, very efficiently identify multiple stellar populations in GCs (see Paper I for a general introduction into the subject).

In other papers (Milone et al. 2015a, Milone et al.2015b, hereafter Papers II and III), we have shown that the combination of the $C_{F275W,\,F336W,\,F438W}$ pseudo-colour with the $m_{F275W} - m_{F814W}$ colour maximizes the separation between stellar populations along the main sequence (MS) and the red giant branch (RGB) and have used this diagram to identify and characterize seven distinct stellar populations in NGC 7089 (Paper II) and at least five populations in NGC 2808 (Paper III). In Paper IV of this series we provided accurate determination of the GC helium abundance and ages of stellar populations in NGC 6352 (Nardiello et al. 2015a), while in Paper V we have exploited the first results from our survey to set constraints on the formation scenarios (Renzini et al. 2015). Other papers of this series include the study of the internal dynamics of multiple populations (Bellini et al. 2015, Paper VI) and of the horizontal branch (HB) morphology (Brown et al. 2016, Paper VII). An early-stage data release of the photometric and astrometric data is provided in Paper VIII by Soto et al. (submitted).

In this paper, we identify and characterize multiple stellar populations along the RGB for the entire sample of 57 GCs. The paper is organized as follows. Data reduction and analysis are briefly described in Section 2. In Section 3, we measure the intrinsic RGB width in $C_{F275W,\,F336W,\,F438W}$ and $m_{F275W} - m_{F814W}$ for all the clusters and we describe how to combine these two quantities to construct 'chromosome maps', which most efficiently identify the distinct stellar populations hosted by each individual GC. The chromosome maps of all the clusters are presented in Section 4. We distinguish between putative first and second generations of stars (respectively 1G and 2G) and measure the fraction of 1G stars over the total cluster population. A group of GCs exhibiting particularly complex chromosome maps and characterized by the presence of a multimodal subgiant branch (SGB) are further investigated in Section 5. In Section 6, we present univariate relations between the global parameters of the host clusters, the RGB width and the population ratio. Summary and conclusions follow in Section 7.

2 DATA AND DATA ANALYSIS

This study is mostly based on data from the *HST* program GO-13297 (PI. G. Piotto) and data from the pilot programs GO-12605 and GO-11233 from the same PI. The aim of these programs is to derive high-precision photometry and astrometry of stars in 57 clusters through the *F275W*, *F336W*, and *F438W* filters of the *HST* Ultraviolet and Visual Channel of the Wide Field Camera 3 (WFC3/UVIS). In addition to data and catalogues illustrated in Paper I, we make use of *F606W* and *F814W* photometry from the Wide Field Channel of the Advanced Camera for Survey (WFC/ACS) which is available for all clusters, mainly from the ACS survey of Galactic GCs (GO-10775, PI. A. Sarajedini, see Sarajedini et al. 2007). In order to improve the quality of the photometry for a few clusters, we have included additional archival WFC3/UVIS images in *F275W*, *F336W*, and *F438W* as reported in Table 1.

Table 1. Description of the archive *HST* images set that has been used in this paper in addition to GO-10775, GO-11233, GO-12605, and GO-13297 data.

Cluster	Date	$N \times$ Exp time	Filter	Instrument	Program	PI
NGC 0104	2002 September 30–November 10	3×150 s + 6×100 s + 10 s	*F435W*	WFC/ACS	9281	J. Grindlay
NGC 0104	2002 September 30–July 07	100 s	*F435W*	WFC/ACS	9443	I. King
NGC 0104	2010 September 28–29	2×580s + 30s	*F336W*	WFC3/UVIS	11729	W. Freedman
NGC 0104	2012 November 14–2013 September 20	9×485 s + 9×720 s	*F336W*	WFC3/UVIS	12971	H. Richer
NGC 5139	2009 July 15	9×350 s + 35 s	*F275W*	WFC3/UVIS	11452	J. K. Quijano
NGC 5139	2010 January 12–July 04	22×800 s	*F275W*	WFC3/UVIS	11911	E. Sabbi
NGC 5139	2011 February 14–March 24	8×800 s	*F275W*	WFC3/UVIS	12339	E. Sabbi
NGC 5139	2009 July 15	9×350 s + 35 s	*F336W*	WFC3/UVIS	11452	J. K. Quijano
NGC 5139	2010 January 10–July 04	19×350 s	*F336W*	WFC3/UVIS	11911	E. Sabbi
NGC 5139	2011 February 14–15	9×350 s	*F336W*	WFC3/UVIS	12339	E. Sabbi
NGC 5139	2012 July 26	8×700 s + 11×10 s	*F336W*	WFC3/UVIS	12802	J. MacKenty
NGC 5139	2009 July 15	35 s	*F438W*	WFC3/UVIS	11452	J. K. Quijano
NGC 5139	2010 January 14–July 04	25×438 s	*F438W*	WFC3/UVIS	11911	E. Sabbi
NGC 5139	2011 February 15–March 24	9×350 s	*F438W*	WFC3/UVIS	12339	E. Sabbi
NGC 5139	2009 July 15	35 s	*F814W*	WFC3/UVIS	11452	J. K. Quijano
NGC 5139	2010 January 10–July 04	27×40 s	*F814W*	WFC3/UVIS	11911	E. Sabbi
NGC 5139	2011 February 15–March 24	9×40 s	*F814W*	WFC3/UVIS	12339	E. Sabbi
NGC 5927	2010 September 01	2×475 s + 30 s	*F336W*	WFC3/UVIS	11729	W. Freedman
NGC 6341	2010 October 11	2×425 s + 30 s	*F336W*	WFC3/UVIS	11729	W. Freedman
NGC 6352	2012 February 13	410 s + 5×400 s	*F336W*	WFC3/UVIS	12746	A. Kong
NGC 6362	2010 August 13	5×450 s + 368 s	*F336W*	WFC3/UVIS	12008	A. Kong
NGC 6397	2010 March 9–11	6×620 s	*F336W*	WFC3/UVIS	11633	R. Rich
NGC 6535	2010 September 04	5×400 s + 253 s	*F336W*	WFC3/UVIS	12008	A. Kong
NGC 6752	2010 May 05	2×500 s + 30 s	*F336W*	WFC3/UVIS	11729	W. Freedman
NGC 6752	2011 May 18–September 04	12×389 s + 6×10 s	*F435W*	WFC/ACS	12254	A. Reiners

All the images have been corrected for the effect of poor charge transfer efficiency following Anderson & Bedin (2010). Photometry has been performed on each individual exposure by using the program img2xym_wfc3uv, which has been developed by Jay Anderson and is similar to the img2xym_WFC program (Anderson & King 2006), but optimized for UVIS/WFC3 data. For saturated very-bright stars the photometry was performed using the method developed by Gilliland (2004), which recovers the electrons that have bled into neighbouring pixels. We refer to Section 8.1 in Anderson et al. (2008) for details on the application of this method.

Stellar positions have been corrected for geometric distortion using the solution by Bellini, Anderson & Bedin (2011). Photometry has been calibrated to the Vega-mag system as in Bedin et al. (2005), by using the photometric zero-points provided by the WFC3/UVIS web page.[1] Stellar proper motions have been obtained as in Anderson & King (2003) and Piotto et al. (2012) by comparing the average stellar positions derived from the WFC3 images in the $F336W$ and $F438W$ bands with those from the catalogues by Anderson et al. (2008). We have included in the following analysis only stars that are cluster members according to their proper motions.

Since we are interested in high-precision photometry, we limited our study to relatively isolated stars with small astrometric uncertainties that are well fitted by the point spread function and selected by following the prescriptions given in Milone et al. (2012b). Finally, the photometry has been corrected for differential reddening that area crucial step in identifying multiple sequences from photometry. To do this, we have used the method by Milone et al. (2012b). In a nutshell, we derived a σ clipped fiducial line of the MS and the SGB of each cluster by putting a spline through the median value of colours and magnitude in progressively narrower magnitude intervals. We have then determined for each star the colour residuals of the closest 50 relatively bright and well-measured MS and SGB stars with respect to the fiducial line. To do this, we have excluded the target star from the calculation of its own differential reddening. We assumed as the differential reddening of each star the median value of such residuals measured along the reddening vector, while the uncertainty on the differential reddening has been derived as in Milone (2015).

3 MULTIPLE POPULATIONS ALONG THE RGB

In the next subsections, we explain how we measured the intrinsic $m_{F275W} - m_{F814W}$ and $C_{F275W,\,F336W,\,F438W}$ RGB width, and used these two quantities to construct the chromosome map of each cluster. We then continue our analysis by using these maps to identify the 1G and 2G stellar populations along the RGB.

3.1 The determination of the RGB colour and pseudo-colour width

The colour broadening of the RGB provides evidence for the presence and diversity of multiple stellar populations in GCs. Indeed, in a simple stellar population (made of chemically homogeneous and coeval stars) the observed RGB width is entirely due to observational errors, whereas the observed RGB width is much wider than expected from photometric errors if multiple stellar populations are present.

The procedure to estimate the RGB width in the m_{F814W} versus $m_{F275W} - m_{F814W}$ and $C_{F275W,\,F336W,\,F438W}$ plots is illustrated in Fig. 1 for the cluster NGC 6723, taken as an example; the procedure is based in part on the naive estimator (Silverman 1986). We started by dividing the RGB into a series of $F814W$ magnitude bins of size δm. The bins are defined over a grid of points separated by intervals of fixed magnitude ($s = \delta m/3$). The procedure is extended to the RGB region fainter than the HB level, where multiple sequences are more clearly visible.

For each bin in $F814W$, we calculated the value of the 4th and the 96th percentile of the $m_{F275W} - m_{F814W}$ and $C_{F275W,\,F336W,\,F438W}$ distributions, to which we associated the mean $F814W$ magnitude of RGB stars in each bin. The resulting envelope of the RGB is represented by the red and blue lines in Fig. 1. The smoothing has been performed by boxcar averaging, where each point has been replaced by the average of the three adjacent points. Due to the small number of upper RGB stars, above the HB level, the red and the blue envelopes in the region have been drawn by eye.

The observed RGB width, $W^{\rm obs}_{C\ F275W,F336W,F438W}$, has been derived as the difference between the $C_{F275W,\,F336W,\,F438W}$ index of the red and blue fiducial lines, calculated 2.0 $F814W$ magnitudes above the MS turnoff, as illustrated in panel (b1) of Fig. 1. The error associated to $W^{\rm obs}_{C\ F275W,F336W,F438W}$ has been determined by bootstrapping with replacements over the sample of RGB stars, then repeated 1000 times. The derived errors refer to one standard deviation of the bootstrapped measurements.

The observed RGB width is partly intrinsic and partly due to observational errors and limited statistics. The intrinsic RGB width, $W_{C\,F275W,\,F336W,\,F438W}$, is calculated by subtracting in quadrature the errors affecting the observed width, which include both photometric errors and errors in the differential-reddening correction. The same procedure was adopted to measure the intrinsic $m_{F275W} - m_{F814W}$ RGB colour width, $W_{m_{F275W}-m_{F814W}}$, as illustrated in panel (a1) of Fig. 1. The results are listed in Table 2 and reveal that for all the analysed GCs, the RGB width is always significantly wider than expected from the errors alone, proving that all 57 GCs host multiple stellar populations.

3.2 The 'chromosome maps' of the multiple stellar populations

We now combine the pieces of information coming from both the m_{F814W} versus $m_{F275W} - m_{F814W}$ colour–magnitude diagram (CMD) and the m_{F814W} versus $C_{F275W,\,F336W,\,F438W}$ diagram to identify the multiple stellar populations in each GC. To this end, we have used the method illustrated in Fig. 1, analogous to the technique introduced in Papers II and III, and illustrated here for the RGB of NGC 6723. Briefly, we have 'verticalized' the two diagrams in such a way that the blue and the red fiducial lines translate into vertical lines. This is obtained by defining for each star:

$$\Delta_{F275W,F814W} = W_{F275W,F814W}\,\frac{X - X_{\rm fiducialR}}{X_{\rm fiducialR} - X_{\rm fiducialB}} \quad (1)$$

$$\Delta_{C\ F275W,F336W,F438W} = W_{C\ F275W,F336W,F438W}\,\frac{Y_{\rm fiducialR} - Y}{Y_{\rm fiducialR} - Y_{\rm fiducialB}}, \quad (2)$$

where $X = (m_{F275W} - m_{F814W})$ and $Y = C_{F275W,F336W,F438W}$ and 'fiducial R' and 'fiducial B' correspond to the red and the blue fiducial lines, respectively, as shown in panels (a2) and (b2) of Fig. 1.

Thus, $\Delta_{F275W,\,F814W} = 0$ and $\Delta_{C\,F275W,\,F336W,\,F438W} = 0$ correspond to stars lying on the corresponding red fiducial line and the

[1] http://www.stsci.edu/hst/acs/analysis/zeropoints/zpt.py

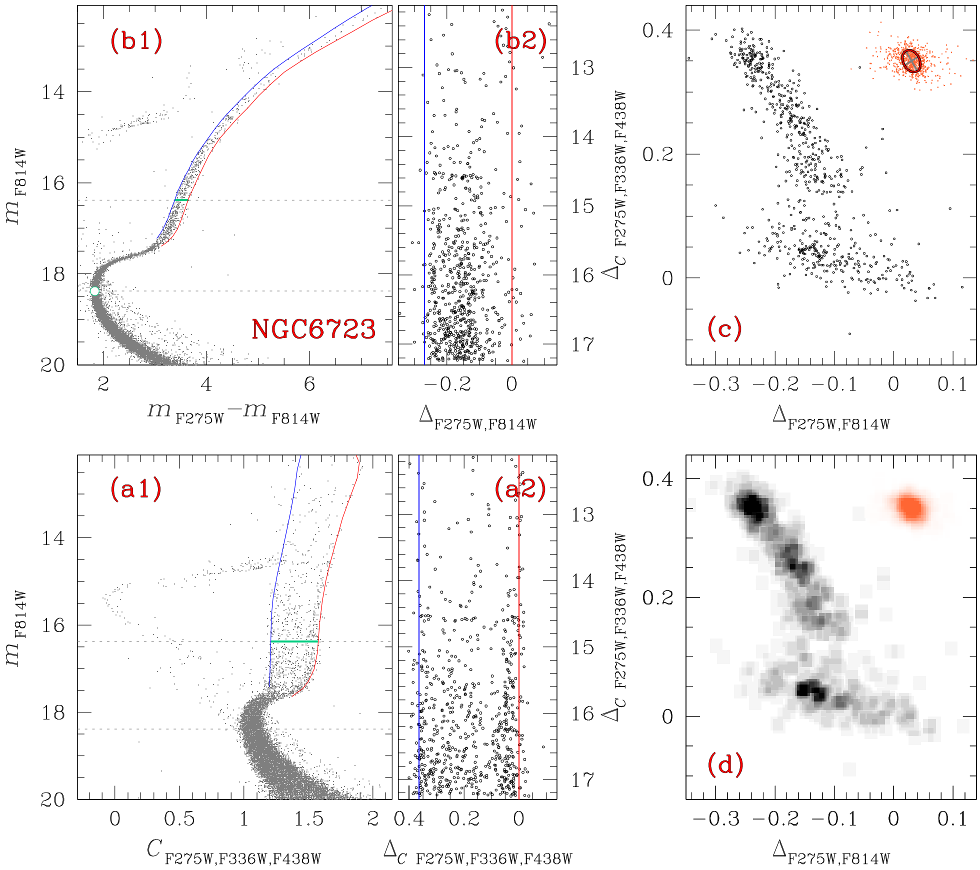

Figure 1. This figure illustrates the procedure to derive the $\Delta_{F275W,\,F336W,\,F438W}$ versus $\Delta_{F275W,\,F814W}$ pseudo-two-colour diagram (or 'chromosome map') for the prototypical cluster NGC 6723. Panels (a1) and (b1) show the m_{F814W} versus $C_{F275W,\,F336W,\,F438W}$ pseudo-CMD and the m_{F814W} versus $m_{F275W} - m_{F814W}$ CMD of NGC 6723. The aqua circle in panel (b1) marks the MS turnoff, whereas the two horizontal dotted lines in panels (a1) and (b1) are placed at the magnitude level of the MS turnoff and 2.0 $F814W$ mag above it. The blue and red lines mark the boundaries of the RGB, while the aqua segments in the panels (a1) and (b1) indicate the $m_{F275W} - m_{F814W}$ colour and the $C_{F275W,\,F336W,\,F438W}$ pseudo-colour separation between the two lines at 2.0 $F814W$ mag above the MS turnoff. The 'verticalized' m_{F814W} versus $\Delta_{C\,F275W,\,F336W,\,F438W}$ and m_{F814W} versus $\Delta_{F275W,\,F814W}$ diagrams for RGB stars are plotted in panels (a2) and (b2), respectively, where the red and blue vertical lines correspond to the RGB boundaries in panels (a1) and (b1) that translate into vertical lines in panel (a2) and (b2). The sample of RGB stars used to construct the chromosome map in panel (c) are those panels (a2) and (b2), where $\Delta_{F275W,\,F336W,\,F438W}$ and $\Delta_{C\,F275W,\,F814W}$ are defined in equations (1) and (2) as explained in the text. The orange points indicate the distribution of stars expected from observational errors only, while the red ellipses include the 68.27 per cent of the points. Panel (d) shows the Hess diagram for stars in panel (c).

Δ quantities represent the colour and pseudo-colour distance from such lines. The resulting $\Delta_{C\,F275W,\,F336W,\,F438W}$ versus $\Delta_{F275W,\,F814W}$ plot is shown in panels (c) and (d) and reveals the distinct stellar populations of NGC 6723.

Following the nomenclature introduced in Paper V, we will refer to plots such as those shown in panels (c) and (d) of Fig. 1 as the 'chromosome map' of a GC. The chromosome maps of all 57 GCs are presented in Section 4.

3.3 Distinguishing first- and second-generation stars

The chromosome map of NGC 6723 shown in panels (c) and (d) of Fig. 1 and in the left-hand panel of Fig. 2 reveals that cluster stars are distributed along two main, distinct groups that we name 1G and 2G and that correspond to the first and second generation of stars as defined in Paper V. It is indeed commonly believed that the multiple stellar populations phenomenon in GCs is the result of multiple events of star formation, where 2G stars form out of material processed by 1G stars (e.g. Decressin et al. 2007, Paper V, D'Antona et al. 2016, and references therein). Thus, in this paper we will consider GC 'multiple populations' and 'multiple generations' as synonyms, as done in previous papers of this series.

We preliminarily identify 1G stars as those at nearly constant $\Delta_{C\,F275W,\,F336W,\,F438W}$ departing from the origin of the reference frame, located at $\Delta_{C\,F275W,\,F336W,\,F438W} = \Delta_{F275W,\,F814W} = 0$. As a consequence, 2G stars are identified as those in the steep branch reaching high values of $\Delta_{C\,F275W,\,F336W,\,F438W}$. A full justification of this choice is presented in Section 4.3, where 1G and 2G are chemically tagged, in analogy to what done in Paper II and Paper III.

The procedure to define a sample of bona fide 1G and 2G stars is illustrated in Fig. 2 for NGC 6723. The green line is a fit to the group of 1G stars and the angle between the green line and the dashed horizontal line is $\theta = 18^{\rm o}$. We adopted this same value of θ for all the analysed clusters. The Δ_2 versus Δ_1 diagram shown in the middle panel of Fig. 2 has been obtained by rotating counterclockwise the left-hand panel diagram by an angle θ around the origin of the reference frame, and the black histogram plotted in the right-hand panel represents the normalized Δ_2 distribution of cluster stars. The orange points shown in the left-hand and middle

Table 2. Values of the RGB width and of the fraction of 1G stars with respect to the total number of analysed stars. We also indicate type-I and type-II clusters and the fraction of type-II stars with respect to the total number of analysed stars. The last two columns provide the number of analysed RGB stars and the ratio between the maximum radial distance from the cluster centre of the analysed stars ($R_{\rm max}$) and the cluster half-light radius ($R_{\rm hl}$). For the type-II clusters, we provide in the second row the values of the RGB width obtained by excluding red-RGB stars ($W^{*}_{C\ F275W,F336W,F438W}$ and $W^{*}_{m_{F275W}-m_{F814W}}$).

ID	$W_{C\ F275W,\ F336W,\ F438W}$	$W_{m_{F275W}-m_{F814W}}$	$W^{\rm 1G}_{m_{F275W}-m_{F814W}}$	$W^{\rm 2G}_{m_{F275W}-m_{F814W}}$	$N_1/N_{\rm TOT}$	Type	$N_{\rm Type\ II}/N_{\rm TOT}$	$N_{\rm stars}$	$R_{\rm max}/R_{\rm hl}$.
NGC 0104	0.369 ± 0.009	0.324 ± 0.019	0.216 ± 0.023	0.164 ± 0.008	0.175 ± 0.009	I	0	1853	0.56
NGC 0288	0.276 ± 0.008	0.174 ± 0.009	0.075 ± 0.008	0.061 ± 0.014	0.542 ± 0.031	I	0	223	0.89
NGC 0362	0.275 ± 0.005	0.192 ± 0.017	0.092 ± 0.012	0.103 ± 0.008	0.279 ± 0.015	II	0.075 ± 0.009	840	2.01
	0.271 ± 0.007	0.187 ± 0.013							
NGC 1261	0.290 ± 0.010	0.203 ± 0.020	0.148 ± 0.025	0.072 ± 0.007	0.359 ± 0.016	II	0.038 ± 0.006	891	2.35
	0.281 ± 0.010	0.203 ± 0.020							
NGC 1851	0.342 ± 0.005	0.206 ± 0.019	0.090 ± 0.010	0.093 ± 0.010	0.264 ± 0.015	II	0.030 ± 0.014	1022	3.00
	0.289 ± 0.010	0.182 ± 0.019							
NGC 2298	0.243 ± 0.017	0.172 ± 0.021	0.139 ± 0.026	0.086 ± 0.014	0.370 ± 0.037	I	0	156	1.61
NGC 2808	0.457 ± 0.009	0.518 ± 0.015	0.183 ± 0.017	0.335 ± 0.011	0.232 ± 0.014	I	0	2682	2.32
NGC 3201	0.292 ± 0.016	0.211 ± 0.012	0.150 ± 0.040	0.111 ± 0.057	0.436 ± 0.036	I	0	169	0.52
NGC 4590	0.132 ± 0.007	0.100 ± 0.005	0.065 ± 0.008	0.068 ± 0.007	0.381 ± 0.024	I	0	330	1.13
NGC 4833	0.260 ± 0.008	0.208 ± 0.015	0.126 ± 0.012	0.134 ± 0.007	0.362 ± 0.025	I	0	401	0.73
NGC 5024	0.209 ± 0.005	0.200 ± 0.014	0.169 ± 0.016	0.096 ± 0.008	0.328 ± 0.020	I	0	1081	1.35
NGC 5053	0.102 ± 0.013	0.072 ± 0.009	0.049 ± 0.012	0.000 ± 0.007	0.544 ± 0.062	I	0	56	0.53
NGC 5139	0.390 ± 0.010	1.090 ± 0.147	0.146 ± 0.011	0.260 ± 0.006	0.086 ± 0.010	II	0.640 ± 0.018	3084	0.50
	0.372 ± 0.010	0.254 ± 0.005							
NGC 5272	0.279 ± 0.007	0.263 ± 0.012	0.244 ± 0.014	0.094 ± 0.006	0.305 ± 0.014	I	0	1177	0.83
NGC 5286	0.303 ± 0.007	0.303 ± 0.021	0.146 ± 0.010	0.138 ± 0.007	0.342 ± 0.015	II	0.167 ± 0.010	1521	2.25
	0.292 ± 0.013	0.249 ± 0.014							
NGC 5466	0.141 ± 0.016	0.108 ± 0.035	0.048 ± 0.029	0.042 ± 0.012	0.467 ± 0.063	I	0	62	0.67
NGC 5897	0.149 ± 0.008	0.121 ± 0.014	0.081 ± 0.019	0.080 ± 0.012	0.547 ± 0.042	I	0	194	0.79
NGC 5904	0.332 ± 0.013	0.219 ± 0.034	0.163 ± 0.033	0.105 ± 0.008	0.235 ± 0.013	I	0	965	0.90
NGC 5927	0.422 ± 0.020	0.745 ± 0.065	0.631 ± 0.066	0.304 ± 0.037	–	I	0	583	1.52
NGC 5986	0.294 ± 0.008	0.222 ± 0.007	0.070 ± 0.006	0.145 ± 0.007	0.246 ± 0.012	I	0	895	1.81
NGC 6093	0.305 ± 0.015	0.246 ± 0.007	0.090 ± 0.008	0.159 ± 0.012	0.351 ± 0.029	I	0	668	2.52
NGC 6101	0.140 ± 0.009	0.116 ± 0.012	0.063 ± 0.013	0.056 ± 0.008	0.654 ± 0.032	I	0	263	1.48
NGC 6121	0.270 ± 0.007	0.161 ± 0.015	0.056 ± 0.045	0.099 ± 0.015	0.285 ± 0.037	I	0	135	0.39
NGC 6144	0.210 ± 0.012	0.160 ± 0.012	0.121 ± 0.023	0.094 ± 0.008	0.444 ± 0.037	I	0	159	0.95
NGC 6171	0.351 ± 0.017	0.220 ± 0.033	0.115 ± 0.020	0.104 ± 0.020	0.397 ± 0.031	I	0	245	0.90
NGC 6205	0.291 ± 0.006	0.231 ± 0.008	0.096 ± 0.020	0.143 ± 0.006	0.184 ± 0.013	I	0	1198	1.05
NGC 6218	0.274 ± 0.009	0.137 ± 0.009	0.073 ± 0.018	0.065 ± 0.015	0.400 ± 0.029	I	0	315	0.93
NGC 6254	0.310 ± 0.007	0.236 ± 0.011	0.156 ± 0.020	0.100 ± 0.008	0.364 ± 0.028	I	0	488	0.86
NGC 6304	0.320 ± 0.024	0.503 ± 0.053	0.371 ± 0.083	0.228 ± 0.028	–	I	0	602	1.13
NGC 6341	0.177 ± 0.005	0.168 ± 0.009	0.078 ± 0.011	0.081 ± 0.003	0.304 ± 0.015	I	0	795	1.63
NGC 6352	0.395 ± 0.015	0.332 ± 0.037	0.193 ± 0.053	0.171 ± 0.041	0.474 ± 0.035	I	0	221	0.76
NGC 6362	0.292 ± 0.011	0.210 ± 0.048	0.093 ± 0.036	0.086 ± 0.010	0.574 ± 0.035	I	0	233	0.81
NGC 6366	0.291 ± 0.064	0.318 ± 0.049	0.043 ± 0.075	0.131 ± 0.037	0.418 ± 0.045	I	0	72	0.51
NGC 6388	0.494 ± 0.010	0.559 ± 0.027	–	–	0.245 ± 0.010	II	0.299 ± 0.016	1735	2.45
NGC 6397	0.117 ± 0.023	0.077 ± 0.009	0.074 ± 0.011	0.031 ± 0.011	0.345 ± 0.036	I	0	111	0.55
NGC 6441	0.512 ± 0.015	0.792 ± 0.025	0.283 ± 0.025	0.298 ± 0.017	–	I	0	1907	2.90
NGC 6496	0.331 ± 0.038	0.311 ± 0.032	0.234 ± 0.033	0.125 ± 0.018	0.674 ± 0.035	I	0	196	1.40
NGC 6535	0.142 ± 0.020	0.110 ± 0.067	0.088 ± 0.015	0.055 ± 0.041	0.536 ± 0.081	I	0	62	1.70
NGC 6541	0.275 ± 0.007	0.214 ± 0.015	0.080 ± 0.009	0.103 ± 0.006	0.396 ± 0.020	I	0	692	1.56
NGC 6584	0.221 ± 0.014	0.153 ± 0.030	0.133 ± 0.031	0.042 ± 0.010	0.451 ± 0.026	I	0	417	2.27
NGC 6624	0.444 ± 0.015	0.436 ± 0.038	0.282 ± 0.040	0.196 ± 0.020	0.279 ± 0.020	I	0	594	1.87
NGC 6637	0.367 ± 0.011	0.283 ± 0.016	0.151 ± 0.022	0.149 ± 0.011	0.425 ± 0.017	I	0	862	2.05
NGC 6652	0.341 ± 0.014	0.277 ± 0.026	0.207 ± 0.027	0.089 ± 0.010	0.344 ± 0.026	I	0	340	3.09
NGC 6656	0.293 ± 0.012	0.344 ± 0.019	0.152 ± 0.030	0.159 ± 0.018	0.274 ± 0.020	II	0.403 ± 0.021	557	0.51
	0.215 ± 0.010	0.234 ± 0.023							
NGC 6681	0.309 ± 0.005	0.208 ± 0.009	0.060 ± 0.013	0.135 ± 0.007	0.234 ± 0.019	I	0	527	2.31
NGC 6715	0.404 ± 0.009	0.388 ± 0.013	0.261 ± 0.016	0.190 ± 0.011	0.267 ± 0.012	II	0.046 ± 0.011	2358	2.08
	0.346 ± 0.012	0.349 ± 0.016							
NGC 6717	0.293 ± 0.012	0.175 ± 0.070	0.029 ± 0.015	0.057 ± 0.018	0.637 ± 0.039	I	0	102	2.01
NGC 6723	0.352 ± 0.006	0.268 ± 0.016	0.195 ± 0.020	0.128 ± 0.009	0.363 ± 0.017	I	0	695	1.05
NGC 6752	0.320 ± 0.015	0.197 ± 0.010	0.100 ± 0.016	0.127 ± 0.008	0.294 ± 0.023	I	0	372	0.91
NGC 6779	0.256 ± 0.007	0.203 ± 0.036	0.090 ± 0.039	0.102 ± 0.013	0.469 ± 0.041	I	0	420	1.29
NGC 6809	0.211 ± 0.012	0.146 ± 0.006	0.086 ± 0.008	0.100 ± 0.010	0.311 ± 0.029	I	0	171	0.55
NGC 6838	0.334 ± 0.014	0.236 ± 0.026	0.165 ± 0.025	0.046 ± 0.015	0.622 ± 0.038	I	0	132	0.88
NGC 6934	0.312 ± 0.015	0.255 ± 0.021	0.123 ± 0.028	0.102 ± 0.016	0.326 ± 0.020	II	0.067 ± 0.010	606	2.30
	0.304 ± 0.013	0.237 ± 0.015							
NGC 6981	0.240 ± 0.009	0.196 ± 0.019	0.142 ± 0.026	0.045 ± 0.018	0.542 ± 0.027	I	0	389	1.67
NGC 7078	0.217 ± 0.003	0.215 ± 0.007	0.102 ± 0.007	0.106 ± 0.005	0.399 ± 0.019	I	0	1495	1.79
NGC 7089	0.302 ± 0.009	0.309 ± 0.014	0.151 ± 0.022	0.166 ± 0.009	0.224 ± 0.014	II	0.043 ± 0.006	1296	1.47
	0.302 ± 0.009	0.309 ± 0.014							
NGC 7099	0.140 ± 0.009	0.122 ± 0.017	0.000 ± 0.010	0.056 ± 0.009	0.380 ± 0.028	I	0	323	1.55

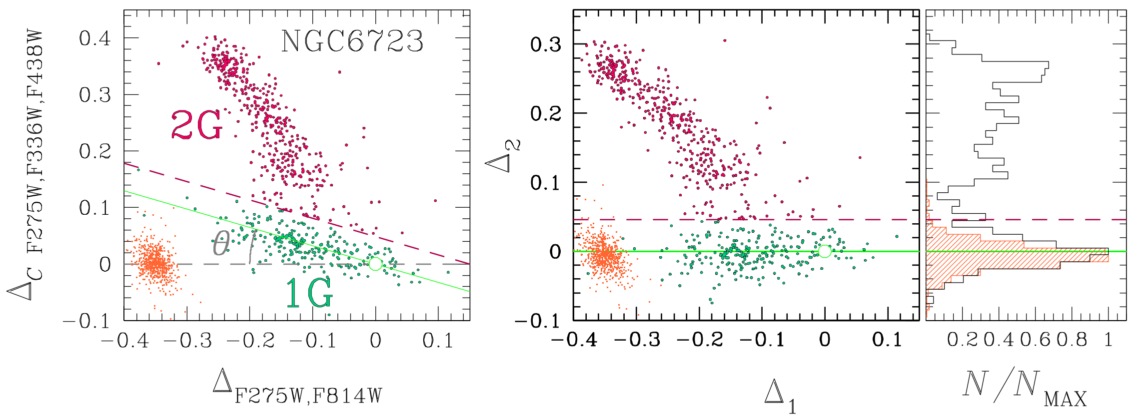

Figure 2. The figure illustrates the method used to identify the two samples of bona fide first-generation (1G) and second-generation (2G) stars in NGC 6723. The left-hand panel reproduces the $\Delta_{F275W,\,F336W,\,F438W}$ versus $\Delta_{F275W,\,F814W}$ diagram from Fig. 1. The green line through the origin of the frame is a fit to the sequence of candidate 1G stars and defines an angle $\theta = 18°$ with respect to the horizontal line. The middle panel shows the Δ_2 versus Δ_1 plot where these new coordinates have been obtained by rotating counterclockwise by an angle θ the plot in the left-hand panel. The histogram in the right-hand panel shows the distributions of the Δ_2 values. The orange points in the left-hand and middle panels show the distribution of the observational errors and their Δ_2 distribution is represented by the shaded orange histogram in the right-hand panel. The dashed magenta lines separate the selected 1G and 2G stars, which are coloured aqua and magenta, respectively, in the left-hand and middle panels. See the text for details.

panels of Fig. 2 represent the expected distribution of the observational errors obtained by Monte Carlo simulations and have been plotted at the arbitrary position $\Delta_2 = 0$. The normalized histogram distribution of the Δ_2 errors is shown in orange in the right-hand panel of the figure. The magenta dashed line is then plotted at the Δ_2 level corresponding to the 3σ deviation from the mean of the error histogram, and the same line is also reported in the left-hand panel, after counter rotation.

We have then taken as bona fide 1G stars all those below the magenta dashed line, while the remaining stars are defined as 2G. 1G and 2G stars are coloured aqua and magenta, respectively, in the left-hand and middle panel of Fig. 2. We can already notice that the $\Delta_{F275W,\,F814W}$ and $\Delta_{C\,F275W,\,F336W,\,F438W}$ extension of both 1G and 2G stars in this cluster is significantly wider than expected from photometric errors alone, thus demonstrating that both 1G and 2G stars in the cluster are not chemically homogeneous. As we shall see, this is the case for the vast majority of our 57 GCs.

4 THE CHROMOSOME MAPS OF THE 57 GLOBULAR CLUSTERS

Figs 3–7 show a collection of the chromosome maps for all 57 GCs studied in this paper. GCs are roughly sorted in order of decreasing metallicity, from the most metal rich (NGC 6624, [Fe/H] = −0.44, Fig. 3) to the most metal poor (NGC 7078, [Fe/H] = −2.37, Fig. 7).

4.1 Classifying clusters in two main types

In most maps, it is possible to easily identify the two main groups of 1G and 2G stars as it was the case for NGC 6723 (see Fig. 2). The magenta dashed lines superimposed on each panel of Figs 3–7 have been derived as described in Section 4.2 and have been used to identify the two groups of bona fide 1G and 2G stars of each cluster. Clusters for which the map allows the 1G/2G distinction as described for NGC 6723 are called here type-I clusters. However, the extension of the 1G group of stars and its separation from the 2G group are quite ambiguous in some clusters, and eventually a distinction between 1G and 2G groups is no longer possible, at least with the present photometric accuracy. This is the case for the three clusters NGC 5927, NGC 6304, and NGC 6441. The 1G/2G separation may still be possible using other passbands, such as in the case of NGC 6441 (Bellini et al. 2013).

Finally, several other clusters exhibit more complex chromosome maps, with an additional 2G sequence (e.g. NGC 1851) or even what appears to be a split of both 1G and 2G sequences (e.g. NGC 6934). Stars in these additional sequences are coloured in red in the chromosome maps. These are the clusters that define the type II and, besides the mentioned NGC 1851 and NGC 6934, this group includes NGC 362, NGC 1261, NGC 5286, NGC 6388, NGC 6656, NGC 6715, NGC 7089, and the famous ω Cen which, not surprisingly, has the most complex map of them all. Noticeably, in order to derive the red and blue fiducial lines that are used to determine the chromosome map of type-II GCs (see Fig. 1), we used only blue-RGB stars. Type-II clusters deserve a dedicated analysis, which is presented in Section 5.

As illustrated by Figs 3–7, the chromosome maps of type-I GC exhibit a great deal of variety. In particular, the $\Delta_{C\,F275W,\,F336W,\,F438W}$ and $\Delta_{F275W,\,F814W}$ extensions differ from one cluster to another, and in several clusters distinct clumps are clearly visible within the 1G and/or the 2G sequences. This is the case of NGC 2808 where at least five distinct subpopulations can be identified, as already illustrated in Paper III. The detailed study of substructures within the 1G and 2G sequences is not further developed in this paper.

Among type-I clusters, quite surprising is the case of NGC 6441, often considered a twin cluster of NGC 6388, since both are metal-rich clusters with an extended blue HB (e.g. Rich et al. 1997; Bellini et al. 2013, and references therein). Yet, their chromosome maps are radically different, with the type-II NGC 6388 exhibiting a very complex map whereas the type-I NGC 6441 shows a unique sequence where it is not even possible to distinguish between 1G and 2G stars. Similarly, we note significant difference between the chromosome map of the second-parameter pair cluster NGC 6205 (M 13) and NGC 5272 (M 3), with the latter hosting a very extended 1G. First- and second-generation stars in the other famous second-parameter pair, NGC 288 NGC 362, share a similar distribution in the corresponding chromosome maps. Intriguingly,

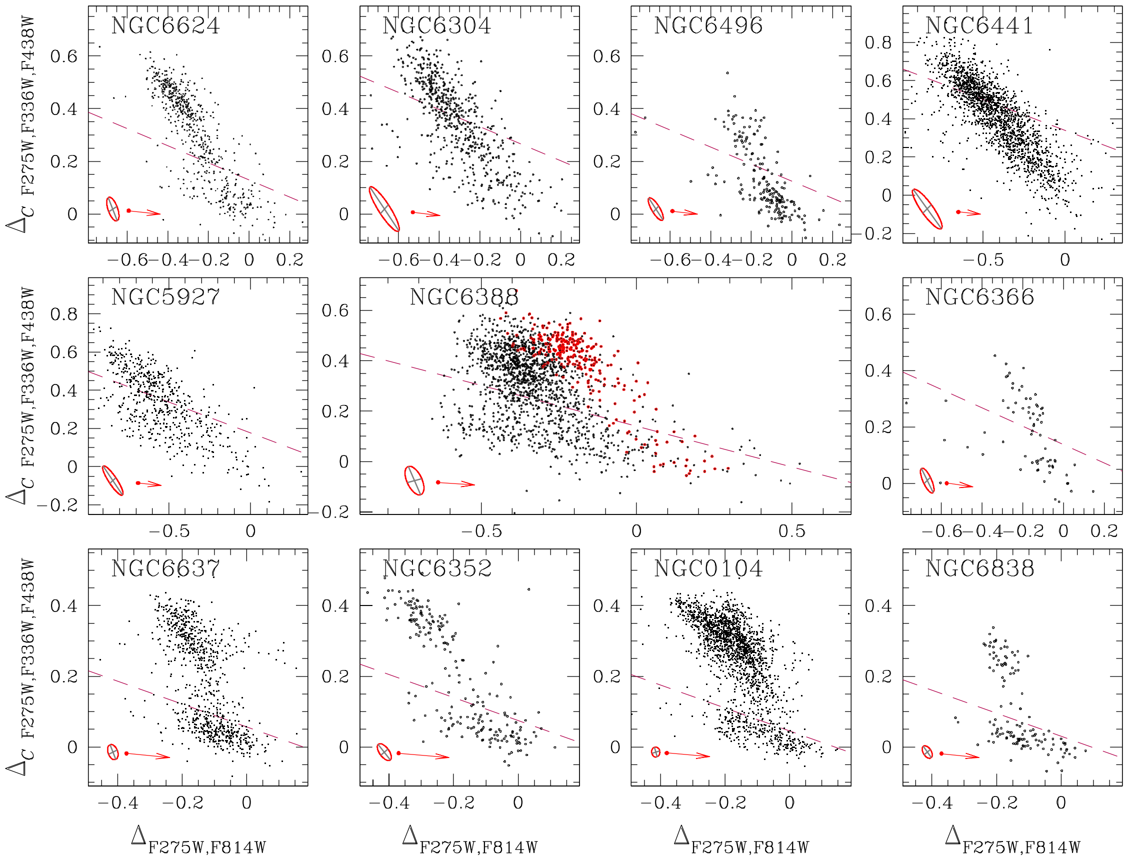

Figure 3. $\Delta_{C\,F275W,\,F336W,\,F438W}$ versus $\Delta_{F275W,\,F814W}$ diagrams, or chromosome maps, for RGB stars in 11 GCs. Namely NGC 6624, NGC 6304, NGC 6496, NGC 6441, NGC 5927, NGC 6388, NGC 6366, NGC 6637, NGC 6352, NGC 104 (47 Tucanae), and NGC 6838 (M 71). Clusters are approximately sorted according to their metallicity, from the most metal rich, to the most metal poor. The ellipses are indicative of the observational errors and include 68.27 per cent of the simulated stars. The magenta dashed line is used to separate bona fide 1G from 2G stars and has been determined as in Section 4.2. Red points indicate red-RGB stars and will be selected and discussed in Section 5, while the arrows indicate the reddening vector and correspond to a reddening variation of $\Delta E(B-V) = 0.05$. Note, however, that all these plots are constructed using photometric data corrected for differential reddening.

NGC 362 hosts a poorly populated red RGB, which is not present in NGC 288.

4.2 The fraction of 1G stars

The procedure to estimate the fraction of 1G stars with respect to the total number of studied RGB stars (N_{TOT}) is illustrated in the upper panels of Fig. 8 for NGC 6723, where we reproduce the Δ_2 versus Δ_1 plot shown in Fig. 2, now having coloured 1G and 2G stars aqua and magenta, respectively. The corresponding histogram distribution of Δ_2 is plotted in the upper-right panel of Fig. 8. The Gaussian fit to the distribution of bona fide 1G stars selected in Section 3.2 is represented by the red continuous line. The fraction of 1G stars (N_1/N_{TOT}) has been derived as the ratio between the area under the Gaussian and the total number of RGB stars in the chromosome map.

The middle panels of Fig. 8 illustrate the procedure described above, now applied to NGC 6205 where the separation between 1G and 2G stars is much less evident than for NGC 6723. NGC 6205 is the most uncertain case for a cluster that we classified as type I. The lower panels of Fig. 8 show the case for NGC 6441, where there is no appreciable separation between 1G and 2G stars, making NGC 6441 a typical example of a type-I cluster for which we did not attempt to estimate the fraction of 1G stars.

The derived fractions of 1G stars are listed in Table 2 which also provides the total number of RGB stars included in the chromosome map and the ratio between the maximum radius of the analysed stars and the cluster half-light radius. Radial gradients in the distribution of the 1G and 2G stars are indeed known to exist in some clusters (e.g. Sollima et al. 2007; Bellini et al. 2009, 2013; Johnson & Pilachowski 2010; Milone et al. 2012b; Cordero et al. 2014), hence this ratio provides a rough indication of the relative number of stars within the analysed field of view with respect to the entire cluster stellar population.

A visual inspection of the maps shown in Figs 3–7 reveals that the $\Delta_{F275W,\,F814W}$ extension of 1G and 2G stars may dramatically differ from one cluster to another. For example, in NGC 6205 and NGC 6752 the second generation is significantly more extended than the first one, while in NGC 5024 and NGC 5272 1G and 2G stars have a similar extension.

In order to quantify the $\Delta_{F275W,\,F814W}$ extension of 1G and 2G stars, we determined the width of the 1(2)G, $W^{\rm obs,1(2)G}_{F275W,F814W}$, as the difference between the 90th and the 10th percentile of the $\Delta_{F275W,\,F814W}$ distribution of 1(2)G stars. The intrinsic width has been estimated by subtracting the colour errors in quadrature (including errors associated with the differential reddening corrections). The values of $W^{\rm 1(2)G}_{F275W,F814W}$ are also listed in Table 2.

As already noted, the fact that $W^{\rm 1(2)G}_{F275W,F814W}$ is significantly larger than zero in most GCs, (i.e. the observed 1G and 2G widths are

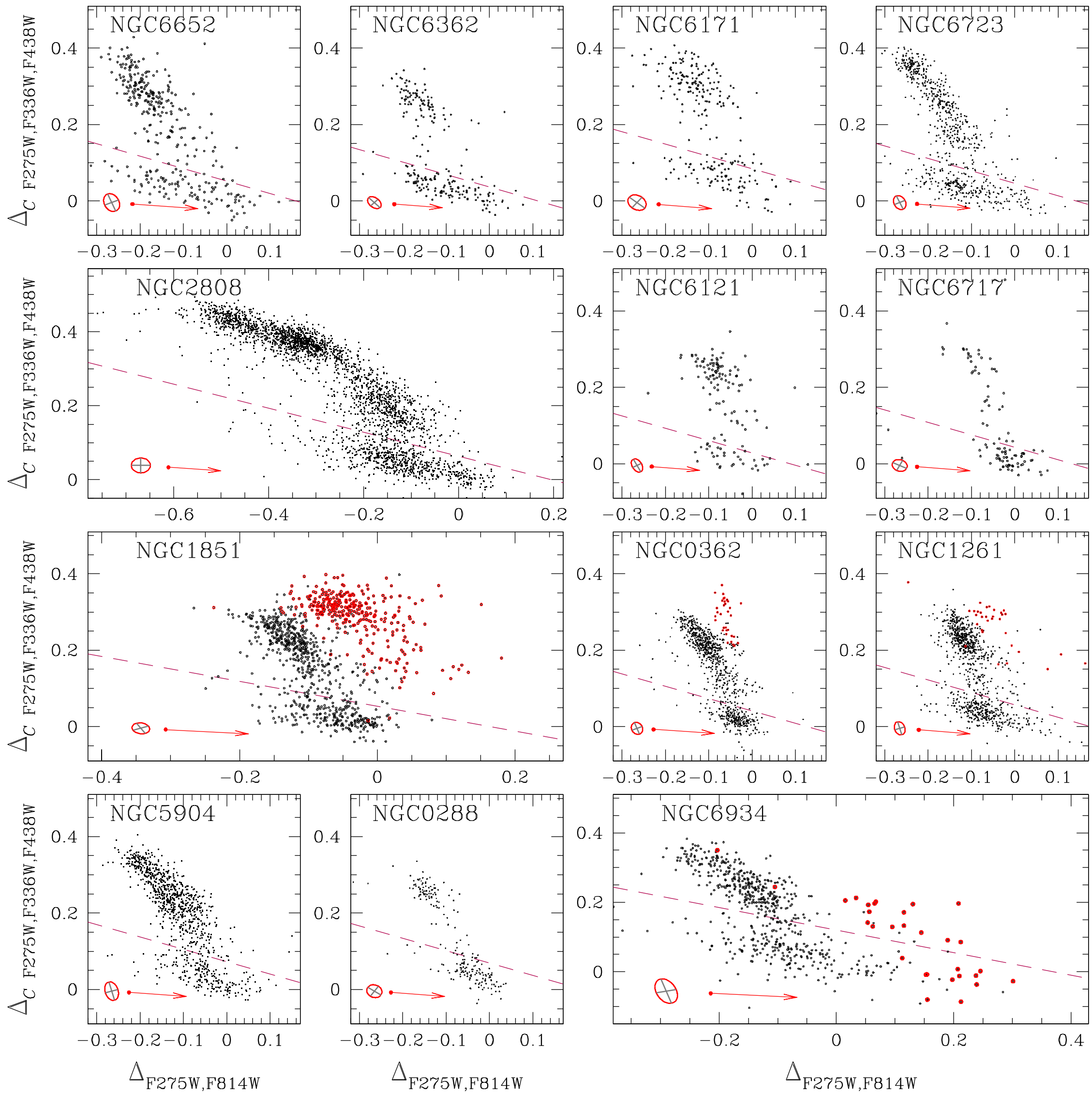

Figure 4. As in Fig. 3, but for NGC 6652, NGC 6362, NGC 6171 (M 107), NGC 6723, NGC 2808, NGC 6121 (M 4), NGC 6717, NGC 1851, NGC 362, NGC 1261, NGC 5904 (M 5), NGC 288, and NGC 6934.

larger than measurement errors) demonstrates that neither 1G nor 2G are consistent with a simple stellar population. This raises a new fundamental question: what are the chemical differences within the 1G population of a GC?

4.3 The chemical composition of multiple stellar populations

The chemical characterization of the multiple populations identified on the chromosome maps is a key step to justify our identification of 1G and 2G stars as belonging to the first and the second generation and an indispensable tool to understand their origin. For this purpose, the spectroscopic analysis of some stars included in our chromosome maps is needed. At present, we can rely only on existing data but additional extensive spectroscopic surveys are needed to shed further light on our photometric data.

To illustrate the case, in Fig. 9 we focus on NGC 6121 as a prototype of a type-I cluster. Multiple stellar populations in NGC 6121 have been widely studied, both photometrically (e.g. Marino et al. 2008; Milone et al. 2014; Nardiello et al. 2015b) and spectroscopically (e.g. Ivans et al. 1999; Marino et al. 2008, 2011; Carretta et al. 2009, 2013). From Marino et al. (2008), chemical analysis is available for 11 stars in common with our WFC3/UVIS sample of RGB stars. Panel (b) of Fig. 9 shows the sodium–oxygen anticorrelation, where some stars are oxygen rich and sodium poor, hence with primordial chemical composition, while others are enhanced in sodium and depleted in oxygen. These stars are shown, respectively, with aqua and magenta filled circles in panels (a) and (b) of Fig. 9, showing that those we have called 1G stars have indeed primordial chemical composition, while 2G stars are Na rich and O poor. No significant differences in iron content appear to exist among 1G and 2G stars in NGC 6121. In Papers II and III, we performed a similar chemical tagging for NGC 7089 and for NGC 2808, by comparing the chromosome map of these clusters with the light-element abundances from Yong et al. (2014) and Carretta et al. (2006), respectively.

The chemical tagging of stars identified on the chromosome maps is clearly very limited at this time, but it could be greatly expanded by future spectroscopic observations targeting stars selected on the

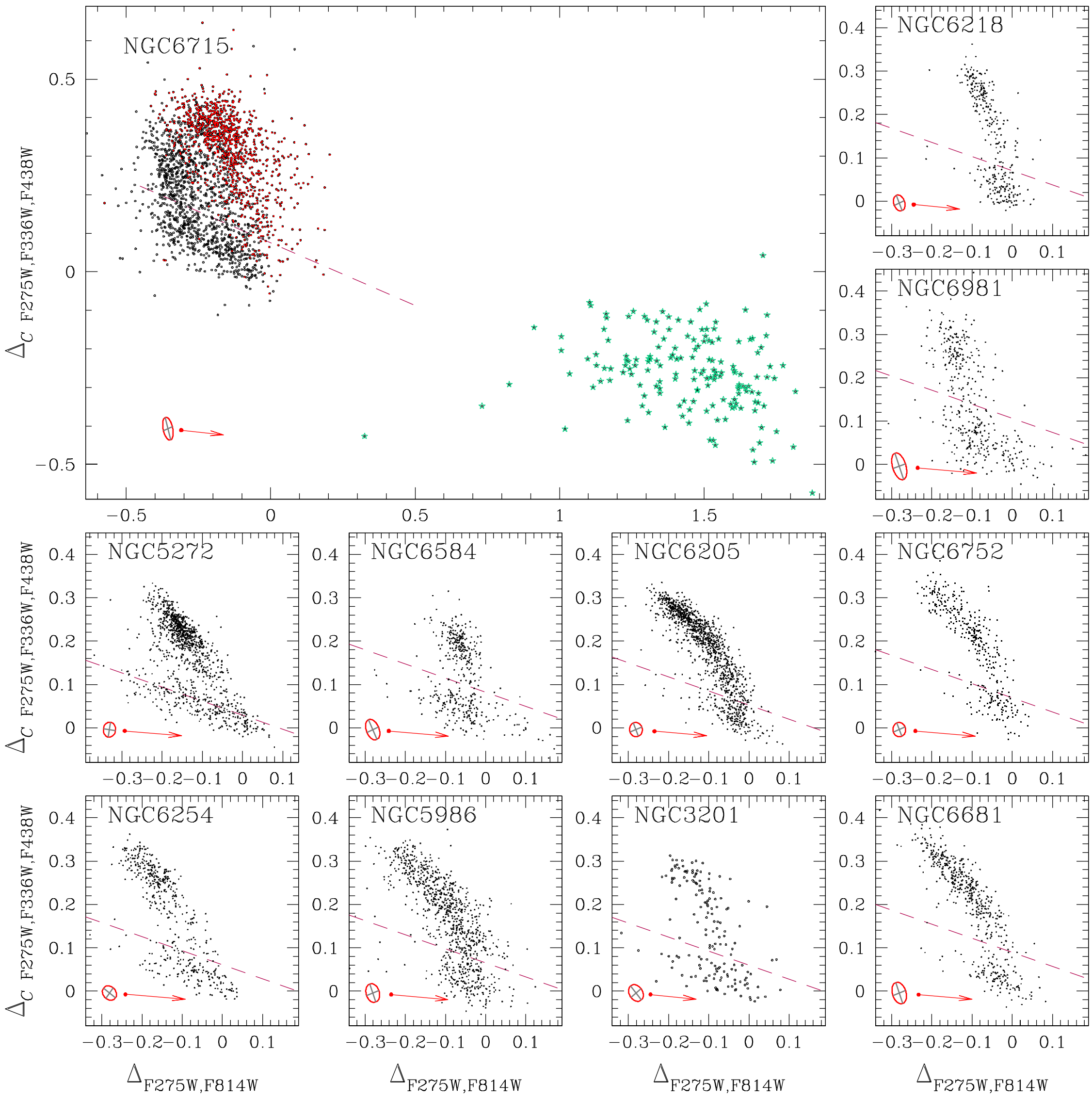

Figure 5. As in Fig. 3, but for the stellar system formed by NGC 6715 (M 54), and for NGC 6218 (M 12), NGC 6981 (M 72), NGC 5272 (M 3), NGC 6584, NGC 6205 (M 13), NGC 6752, NGC 6254 (M 10), NGC 5986, NGC 3201, and NGC 6681 (M 70). The aqua-starred symbols in the map of M 54 indicate stars of the metal-rich population in the core of the Sagittarius dwarf galaxy, to which M54 belongs.

chromosome maps illustrated in this paper. The other panels in Fig. 9 refer to the type-II GC NGC 5286 and will be used in the next section dedicated to type-II clusters.

5 GLOBULAR CLUSTERS OF TYPE II

In this section, we present additional evidence to further explore and characterize the stellar-population content of type II GCs, the most complex ones. A visual inspection of the chromosome map of NGC 1851 (Fig. 4) reveals that the map itself appears to be split, with two 2G sequences running vaguely parallel to each other, and a hint of a second 1G sequence as well. To better understand the origin of such a complex pattern, in Fig. 10 we show a collection of CMDs for NGC 1851. The CMD in the upper panel reveals that the SGB is clearly split into a bright and faint SGB (red points in the insert for the latter) which are connected to the blue and the red RGB, respectively. The RGB splitting was first noticed by Han et al. (2009) using ground-based U versus $U - I$ photometry. The red-RGB stars have been coloured red in the upper panel of Fig. 10.

We used the same colours to represent the sample of selected faint-SGB stars in the m_{F438W} versus $m_{F438W} - m_{F814W}$, $m_{\rm F606W}$ versus $m_{\rm F606W} - m_{F814W}$, and m_{F275W} versus $m_{F275W} - m_{F814W}$ CMDs, plotted in the lower panels of Fig. 10. These CMDs not only demonstrate that the split SGB of NGC 1851 is real, but also show that the faint SGB is visible also in CMDs made with optical filters, like m_{F606W} versus $m_{F606W} - m_{F814W}$, where stellar colours and luminosities are not significantly affected by light-element abundance variations (see also Milone et al. 2008). This indicates that faint-SGB stars are either enhanced in their C+N+O overall abundance, or are older than stars on the bright SGB by ∼1–2 Gyr (Cassisi et al. 2008; Ventura et al. 2009; Marino et al. 2011). We emphasize that all type-II clusters exhibit either split or multimodal SGBs when observed in both ultraviolet and optical filters, in contrast to type-I GCs, where multiple populations along the SGB are visible only in

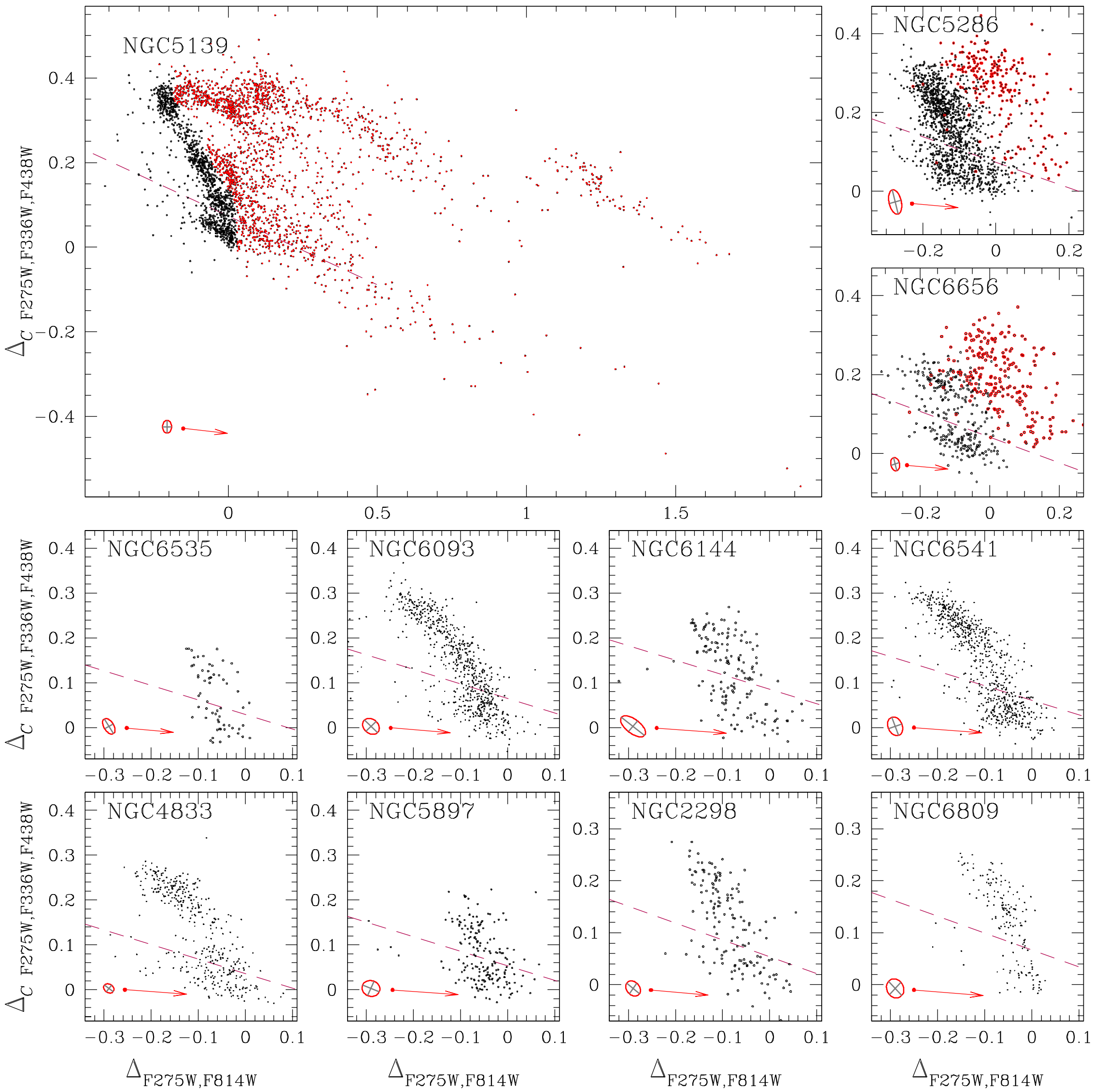

Figure 6. As in Fig. 3, but for NGC 5139 (ω Centauri), NGC 5286, and NGC 6656 (M 22), NGC 6535, NGC 6093 (M 80), NGC 6144, NGC 6541, NGC 4833, NGC 5897, NGC 2298, and NGC 6809 (M 55).

CMDs that include ultraviolet bands (Milone et al. 2008; Marino et al. 2009; Piotto et al. 2012).

A collection of CMDs for other type-II clusters (namely, NGC 362, NGC 1261, NGC 5139, NGC 5286, NGC 6656, NGC 6715, NGC 6093, and NGC 7078) is provided in Figs 11–18. Every CMD shows the existence of a faint SGB that evolves into a red RGB in the m_{F336W} versus $m_{F336W} - m_{F814W}$ CMD. As shown in Fig. 16, the faint-SGB–RGB connection is unclear for NGC 6388 where the RGB split is visible only for stars brighter than $m_{F336W} \lesssim 20.75$. Another possible exception is 47 Tucanae, in which there is no clear connection between multiple populations along the faint SGB and the RGB (Milone et al. 2012b). The red-RGB stars identified in Figs 11–18 are coloured in red in the chromosome maps shown in Figs 3–7. The fact that red-RGB stars are clearly separated from the majority of cluster members in the chromosome maps demonstrates that the $\Delta_{C\,F275W,\,F336W,\,F438W}$ versus $\Delta_{F275W,\,F814W}$ diagram is an efficient tool to identify GCs with multiple SGBs in the optical bands.

The fraction of red-RGB stars with respect to the total number of analysed RGB stars differs significantly from one type-II cluster to another, and ranges from a minimum of ~4 per cent for NGC 1261 and NGC 7089 to a maximum of ~46 per cent and ~64 per cent for NGC 6715 and NGC 5139 (ω Centauri), coming almost to dominate the cluster. Given its complexity, the special case of ω Centauri requires a somewhat more elaborate procedure for the measurement of the RGB width and the construction of its chromosome map, which is illustrated in Appendix A.

For type-II GCs, we have determined the RGB widths $W_{C\,F275W,\,F336W,\,F438W}$ and $W_{m_{F275W}-m_{F814W}}$ as described in Section 3.2 for NGC 6723, but both by using only stars belonging to the blue RGB and by using all the RGB stars. The latter quantities are called $W^{*}_{C\ F275W,F336W,F438W}$ and $W^{*}_{m_{F275W}-m_{F814W}}$. Both W and W^{*} width values are reported in Table 2, with W^{*} values given in a second row for each of the type-II clusters.

In order to illustrate the chemical tagging of multiple populations in type-II clusters, we use NGC 5286 as a prototype. In panel (c)

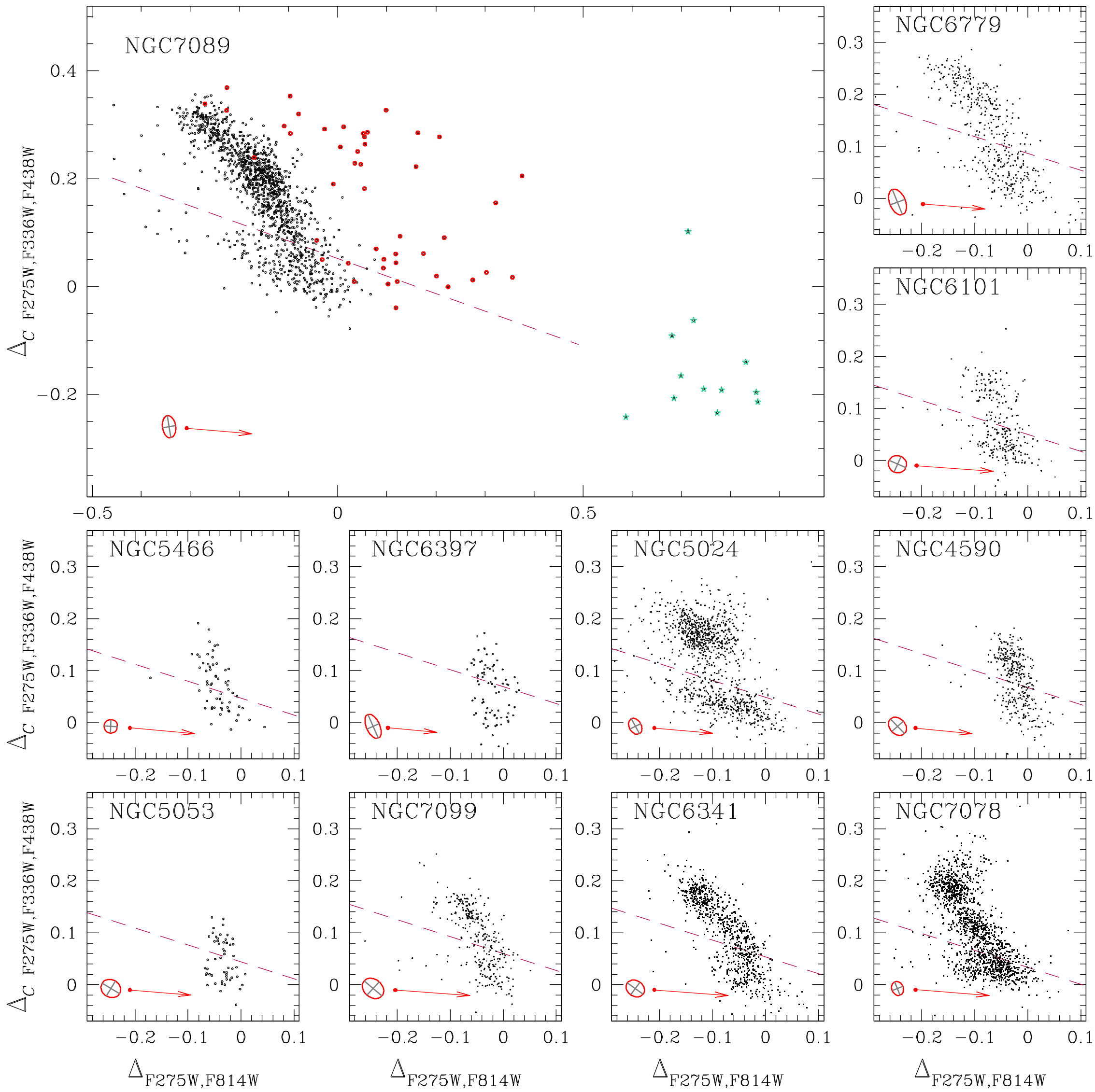

Figure 7. As in Fig. 3, but for NGC 7089 (M 2), NGC 6779 (M 56), NGC 6101, NGC 5466, NGC 6397, NGC 5024, NGC 4590, NGC 5053, NGC 7099 (M 30), NGC 6341 (M 92), and NGC 7078 (M 15). Stars in the most metal-rich population of NGC 7089 are represented with aqua-starred symbols.

of Fig. 9, red-RGB stars of this cluster are coloured red whereas large black filled circles and red triangles are used for those stars for which Marino et al. (2015) have measured their content of iron and s-process-elements, as shown in panel (d). Stars with low iron and barium belong to the 1G and 2G of the blue RGB, coloured in black, while the stars enhanced in [Fe/H] and [Ba/Fe] populate the red RGB.

In panels (a) and (c) of Fig. 19 we show separately the stars of the blue and the red RGBs of NGC 5286, and compare the position of stars in the chromosome map and in the Na–O plot, in close analogy with what was previously done for NGC 6121. We find that both RGBs host 1G stars with primordial oxygen and sodium abundance, and 2G stars enriched in sodium and depleted in oxygen, as shown in panels (b) and (d). In Panel (c), we indicate 1G and 2G stars of the red RGB as 1G,r and 2G,r, respectively. This finding is consistent with the conclusion by Marino et al. (2015) that both the group of barium-rich and barium-poor stars of NGC 5286 exhibit their own Na–O anticorrelation. In Paper II, we have reached a similar conclusion for NGC 7089, using the abundances of light elements, s-process elements, and [Fe/H] from Yong et al. (2014). NGC 7089 hosts a population of stars highly enhanced in iron with respect to the majority of cluster members. Stars in the extreme population of NGC 7089 and the metal-rich stars in the core of the Sagittarius dwarf galaxy which are within the WFC3/UVIS images of NGC 6715 have been represented with aqua-starred symbols in the corresponding chromosome maps.

One intriguing discovery of the last decade is that a small but still increasing number of GCs host two or more distinct groups of stars with different content of iron and s-process elements (Johnson et al. 2015; Marino et al. 2015; Yong, Da Costa & Norris 2016, and references therein), while the majority of clusters have in general homogeneous abundances of s-process elements and metallicity. Moreover, the s-process-rich stars are also iron rich and, in the cases of NGC 6656, NGC 1851, and ω Centauri, these stars are also enhanced in their overall C+N+O abundance (Yong et al. 2009, 2014; Marino et al. 2011, 2012, 2015; Villanova et al. 2014).

The chemical tagging of multiple populations is still quite fragmentary, especially for type-II clusters. However, all the available

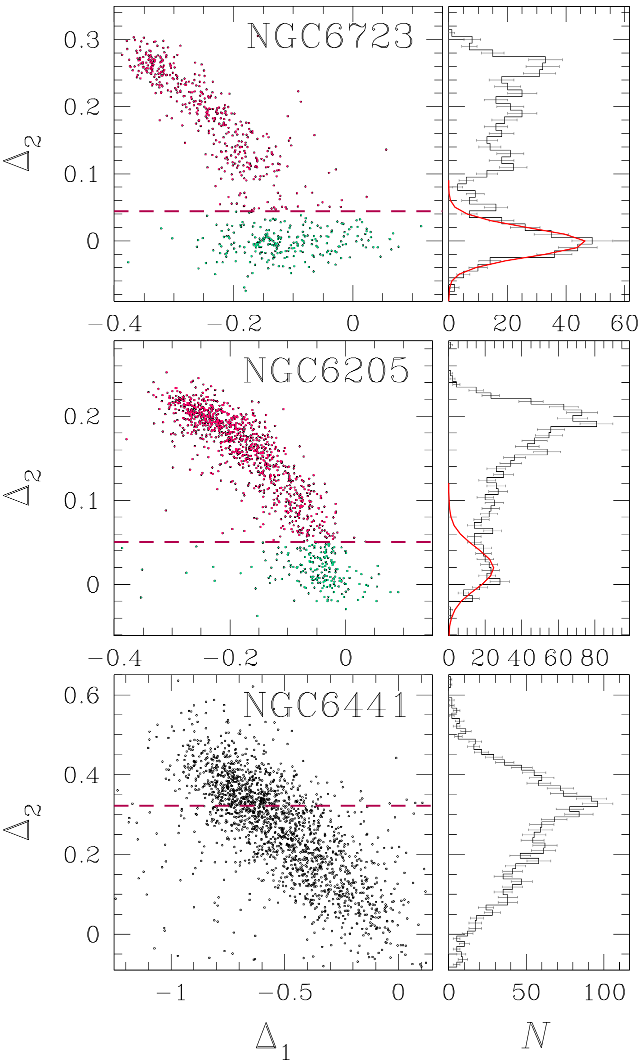

Figure 8. This figure exemplifies the procedure to estimate the fraction of 1G stars with respect to the total number of RGB stars, for NGC 6723 (upper panels) and NGC 6205 (middle panels). The left-hand panels show the Δ_2 versus Δ_1 diagrams presented in Section 4.2, where the pre-selected 1G and 2G stars are coloured aqua and magenta, respectively. The histogram in the right-hand panels show the distributions of the Δ_2 values. The red lines superimposed on the histograms of NGC 6723 and NGC 6205 are the best-fitting Gaussians of the 1G peak of the histogram. The fraction of 1G stars is then calculated as the ratio of the area of the Gaussian over that of the whole histogram. Lower panels show the case of NGC 6441, a type-I cluster, for which no clear distinction can be made between 1G and 2G stars and, correspondingly, we did not estimate the fraction of 1G stars. See the text for details.

evidence indicates that stars in the faint SGB and red RGB are enhanced in global C+N+O content, in iron and in s-process elements. We conclude that type-II clusters differ from type I ones in three aspects: the SGB of type-II GCs splits in optical bands, they host multiple 1G and/or 2G sequences in the chromosome maps and they show a wide composition range in heavy elements. Of course, these three characteristics ought to be physically connected to each other. To the best of our current understanding, each of these three properties, separately, is sufficient to identify as such a type-II cluster. We refer the reader to paper by Marino et al. (2015) and reference therein for further discussion on the chemical composition of type-II GCs.

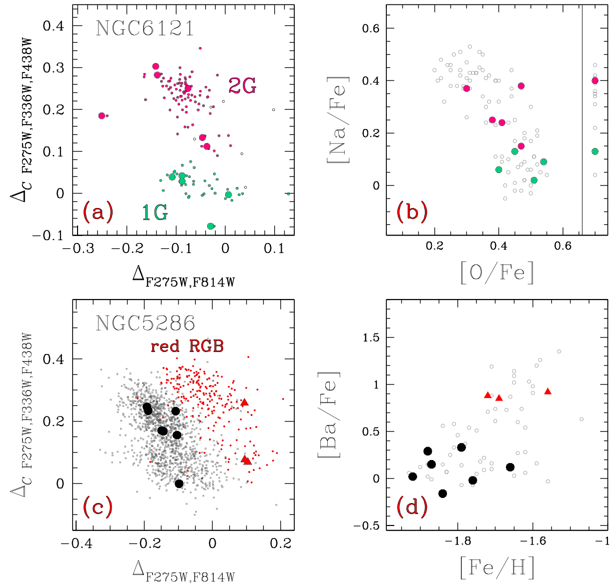

Figure 9. Panel (a) shows the chromosome map of RGB stars in the type I cluster NGC 6121, where we have coloured aqua and magenta 1G and 2G stars, respectively. Large aqua and magenta dots indicate 1G and 2G stars studied spectroscopically by Marino et al. (2008), and whose [Na/Fe] versus [O/Fe] anticorrelation is shown in panel (b) using the same symbols. Stars for which an oxygen abundance determination is not available are plotted on the right side of the vertical line in this and in similar panels. The chromosome map of the type II NGC 5286 is shown in panel (c), where red-RGB stars are coloured red and black point are used for the remaining RGB stars. Large black circles and red triangles indicate those stars studied spectroscopically by Marino et al. (2015), and whose [Ba/Fe] versus [Fe/H] plot is shown in panel (d).

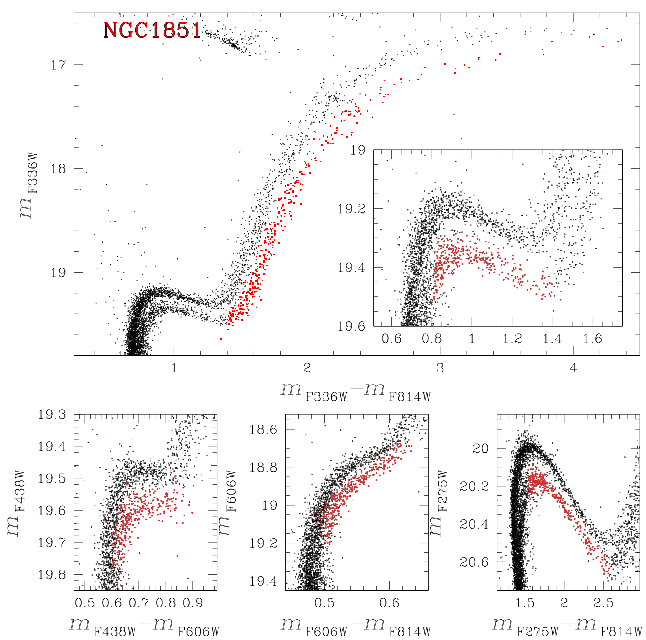

Figure 10. Upper panel: the m_{F336W} versus $m_{F336W}-m_{F814W}$ CMD of NGC 1851 with red-RGB stars coloured red. The inset shows a zoomed-in view around the SGB. Lower panels: m_{F438W} versus $m_{F438W}-m_{F814W}$ (left), $m_{\rm F606W}$ versus $m_{\rm F606W}-m_{F814W}$ (middle), and m_{F275W} versus $m_{F275W}-m_{F814W}$ (right) CMDs around the SGB. The sample of faint SGB stars selected from the CMD in the insert of the upper panel are coloured red in these panels.